to suggest an increased cooling rate of the global surface and troposphere, because their estimated ~5 W/m² increase in OLR radiation (implied cooling) over the period 1985–2000 is larger than the ~2 W/m² SW decrease (implied warming) over the same period (*11*, *13*). Our results for SW radiation are broadly consistent with these studies on a quasi-global scale, although we are somewhat biased toward the tropical regions because of the geometry inherent in ES measurements (Fig. 1). However, the albedo decrease of the proxy is two to three times larger than the satellite estimates, making it comparable to their estimated decrease in OLR (*11*). The post-1999 recovery we find is a novel result.

The effect of clouds on Earth's albedo is probably larger in visible light than in the ultraviolet (UV) or near-IR. For UV radiation, strong Rayleigh scattering and ozone absorption reduce the impact of clouds on the albedo. In the near-IR region, absorption by cloud particles, water vapor, and carbon dioxide all limit the impact. Consequently, variations in broadband SW albedo may be somewhat smaller than those in the visible albedo shown in Fig. 3.

If the changes in cloud properties responsible for the reflectance changes shown by the proxy were a result of secularly increasing atmospheric greenhouse gases, then they would signal a strong positive SW cloud feedback, although a simultaneous negative feedback may be expected through reduced cloud trapping of IR radiation (*14*). However, the reflectance increase from 1999 to 2003 would be difficult to attribute to monotonically increasing atmospheric greenhouse gases. Natural variability is a much more plausible explanation, given the size and time scale of the proxy changes.

We have used a combination of ES and satellite observations to deduce interannual and decadal variations in Earth's large-scale reflectance. A decreasing reflectance since 1984 is derived from the ISCCP data, with a sharp drop during the 1990s. However, the ES data available for subsequent years, with as yet no corresponding ISCCP data, indicate that the trend has reversed since 1999, with the decline being largely erased by the end of 2003. These large variations in reflectance imply climatologically significant cloud-driven changes in Earth's radiation budget, which is consistent with the large tropospheric warming that has occurred over the most recent decades. Moreover, if the observed reversal in Earth's reflectance trend is sustained during the next few years, it might also play a very important role in future climate change. The ability of climate models to reproduce changes such as these (whether due to natural variability or anthropogenic forcing) is therefore an important test of our ability to assess and predict climate change.

**References and Notes**
1. J. Lean, *Annu. Rev. Astron. Astrophys.* **35**, 33 (1997).
2. R. D. Cess et al., *J. Geophys. Res.* **101**, 12791 (1996).
3. The ERBE instruments were flown on the ERBS, NOAA-9, and NOAA-10 satellites from late 1984 to 1990 (asd-www.larc.nasa.gov). ScaRab/Meteor and ScaRaB/Ressur also measured Earth's albedo during 1994–1995 and 1998–1999, respectively (www.lmd.polytechnique.fr/~Scarab/). In 1998, CERES began taking albedo measurements (asd-www.larc.nasa.gov/ceres/), and the Geostationary Earth Radiation Budget Experiment (GERB), the first broadband radiometer on a geostationary satellite, has been in operation since December 2002 (www.sp.ph.ic.ac.uk/gerb/). The future satellite missions EARTHSHINE (www.sstd.rl.ac.uk) and TRIANA (on hold) (triana.gsfc.nasa.gov) may also contribute by observing the full Earth disk reflectance from the privileged deep-space position of the L1 Lagrange point.
4. P. R. Goode et al., *Geophys. Res. Lett.* **28**, 1671 (2001).
5. When referring to SW reflectance as observed by ES, we mean the visible region from 400 to 700 nm covered by our detector.
6. J. Qiu et al., *J. Geophys. Res.* **108**, 4709, 10.1029/2003JD003610 (2003).
7. E. Pallé et al., *J. Geophys. Res.* **108**, 4710, 10.1029/2003JD003611 (2003).
8. W. B. Rossow, A. W. Walker, D. E. Beuschel, M. D. Roiter, *International Satellite Cloud Climatology Project (ISCCP): Documentation of New Cloud Data-sets* (WMO/TD-No. 737, World Meteorological Organization, Geneva, Switzerland, 1996).
9. The latest ISCCP data, documentation, and related information can be downloaded from the ISCCP Web site at http://isccp.giss.nasa.gov.
10. Intergovernmental Panel on Climate Change (IPCC), *Climate Change 2001: The Scientific Basis. Contribution of Working Group I to the Third Assessment Report of the Intergovernmental Panel on Climate Change (IPCC)*, J. T. Houghton et al., Eds. (Cambridge Univ. Press, Cambridge, 2001).
11. B. A. Wielicki et al., *Science* **295**, 841 (2002).
12. P. Wang, P. Minnis, B. A. Wielicki, T. Wong, L. B. Vann, *Geophys. Res. Lett.* **29**, 10.1029/2001GL014264 (2002).
13. J. Chen, B. E. Carlson, A. D. Del Genio, *Science* **295**, 838 (2002).
14. R. D. Cess, P. M. Udelhofen, *Geophys. Res. Lett.* **30**, 1019 (2003).
15. This research was supported in part by a grant from NASA (NAG5-11007). The cloud ISCCP D1 data sets were obtained from the NASA Langley Research Center Atmospheric Sciences Data Center. We are grateful to Y. Yung, B. Soden, T. Schneider, and five anonymous referees for their comments on drafts of this paper.

# Elastic Behavior of Cross-Linked and Bundled Actin Networks

M. L. Gardel,[1] J. H. Shin,[3,4] F. C. MacKintosh,[5] L. Mahadevan,[2] P. Matsudaira,[4] D. A. Weitz[1,2]*

Networks of cross-linked and bundled actin filaments are ubiquitous in the cellular cytoskeleton, but their elasticity remains poorly understood. We show that these networks exhibit exceptional elastic behavior that reflects the mechanical properties of individual filaments. There are two distinct regimes of elasticity, one reflecting bending of single filaments and a second reflecting stretching of entropic fluctuations of filament length. The mechanical stiffness can vary by several decades with small changes in cross-link concentration, and can increase markedly upon application of external stress. We parameterize the full range of behavior in a state diagram and elucidate its origin with a robust model.

Actin is a ubiquitous protein that plays a critical role in virtually all eukaryotic cells. It is a major constituent of the cytoskeletal network that is an essential mechanical component in a variety of cellular processes, including motility, mechanoprotection, and division (*1*, *2*). The mechanical properties, or elasticity, of these cytoskeletal networks are intimately involved in determining how forces are generated and transmitted in living cells. In vitro, actin can polymerize to form long rigid filaments (F-actin), with a diameter $D \approx 7$ nm and contour lengths up to $L \approx 20$ μm (*3*). Despite their rigidity, thermal effects nevertheless modify the dynamic configuration of actin filaments, leading to bending fluctuations. The length scale where these fluctuations completely change the direction of the filament is the persistence length, $\ell_p = \kappa_o/k_B T \approx 17$ μm, determined when the bending energy equals the thermal energy; here, $\kappa_o$ is the bending modulus of the actin filament. Entangled solutions of F-actin are a well-studied model for semiflexible polymers; they exhibit exceptionally large elasticity at small volume fractions as compared with more traditional flexible polymers at similar concentrations (*4*–*6*). However, in vivo, the cytoskeletal network is regulated and controlled not only by the concentration of F-actin, but also by accessory proteins that bind to F-actin. Indeed, nature provides a host of actin-binding proteins (ABPs) with a wide range of functions: They can align actin filaments into bundles and they can cross-link filaments or bundles into networks (*2*, *7*). However, unlike flexible polymers, where changes in cross-link density do not markedly affect the elasticity (*8*), small changes in the concentration of cross-linker ABPs dramatically alter the elasticity of F-actin

[1]Department of Physics, [2]Division of Engineering and Applied Sciences, Harvard University, Cambridge, MA 02138, USA. [3]Department of Mechanical Engineering, Massachusetts Institute of Technology (MIT), Cambridge, MA 02139, USA. [4]Department of Biology and Division of Biological Engineering, Whitehead Institute for Biomedical Research, MIT, Cambridge, MA 02142, USA. [5]Division of Physics and Astronomy, Vrije Universiteit, Amsterdam, Netherlands.

*To whom correspondence should be addressed. E-mail: weitz@deas.harvard.edu

networks (4–6, 9–11). A quantitative understanding of this behavior is essential to control and exploit biomimetic materials based on actin or other semiflexible polymer networks. It is also an essential first step in understanding the elasticity of cytoskeletal networks and the pivotal role of ABPs in the mechanical behavior of the cell. However, very little is known about the microscopic mechanisms underlying the elasticity of semiflexible polymer networks and, in particular, the quantitative behavior of cross-linked and bundled F-actin networks.

We study the elasticity of a model composite network of bundled and cross-linked F-actin. We use an ABP that simultaneously bundles and cross-links actin filaments while being sufficiently rigid so as not to contribute to the network compliance. The elastic behavior of such in vitro networks exhibits marked variation as the F-actin and cross-link densities are varied. For example, by changing the cross-link concentration alone, the network elastic modulus can be reliably and precisely tuned over more than three decades (Fig. 1A); this is in marked contrast to conventional flexible polymer materials, where the elasticity is rather insensitive to chemical cross-links (8). In addition, the network can exhibit considerable stiffening with applied stress, with the effective elasticity increasing by more than a decade with virtually no change in strain; thus, the compliance nearly vanishes. By contrast, at lower concentrations of either F-actin or cross-links, the nonlinear strain stiffening completely disap-

pears, and the network elasticity can remain linear for strains as large as unity. Thus, there are two qualitatively distinct regimes of elasticity, highlighted by the different-colored regions of the state diagram in Fig. 1A. A robust model elucidates the fundamental mechanisms of the network elasticity in each regime and rationalizes both the linear and nonlinear behavior of the elasticity captured by the state diagram (12–14).

The actin cytoskeleton is a highly dynamic and complex network, in which ABPs play a myriad of roles (2, 7). Most ABPs implicated in cross-linking or bundling the network are themselves highly dynamic and compliant, making it extremely difficult to isolate the origins of elasticity of the F-actin network itself (5, 9, 10, 15). To overcome these difficulties, and define a benchmark for the elasticity of cross-linked actin networks, we use scruin, which is found in the sperm cell of the horseshoe crab (16). Scruin-calmodulin dimers decorate individual F-actin filaments, and nonspecific scruin-scruin interactions cross-link and bundle neighboring filaments (17). In vivo, scruin mediates the formation of a single, crystalline bundle of 80 actin filaments; this functions as a mechanochemical spring in the acrosomal process (16, 18). In vitro, actin filaments polymerized in the presence of scruin are cross-linked and bundled by scruin-scruin contacts and form an isotropic, disordered three-dimensional network that is macroscopically homogeneous over a large range of cross-linking concentrations (19). Scruin bonds are irreversible, and scruin itself is

not compliant; thus, the elasticity of our networks appears to be due entirely to the F-actin filaments.
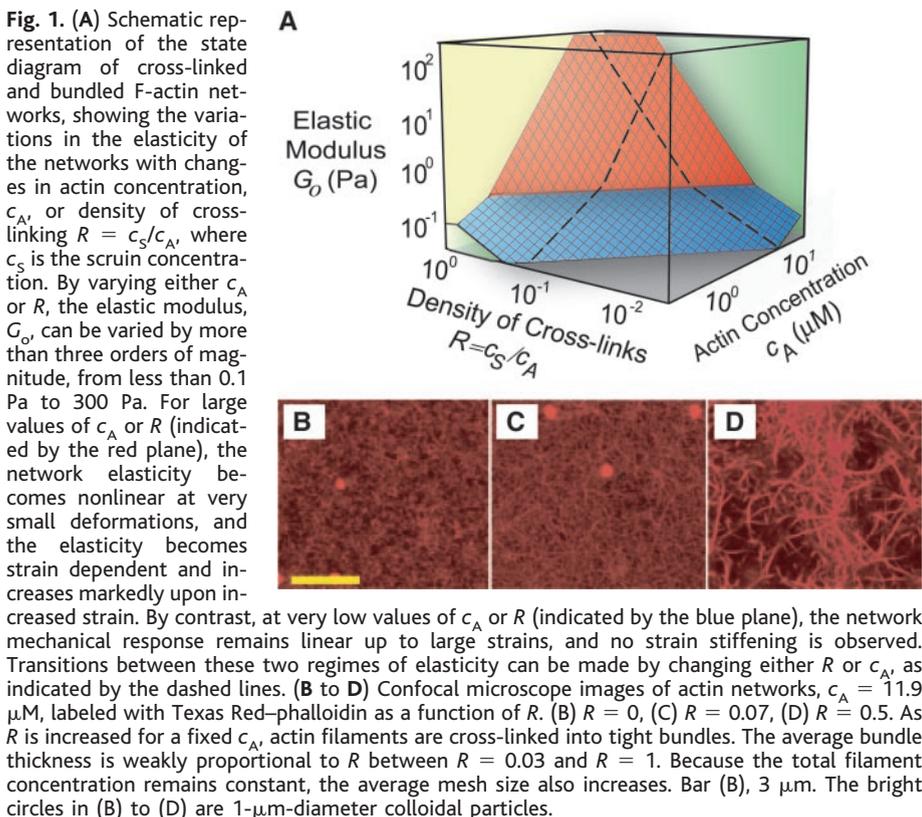
In the absence of scruin, an F-actin solution forms an isotropic and homogeneous mesh; at a concentration of 11.9 μM, the mean separation between filaments is ~300 nm (Fig. 1B). (20). We tune the degree of filament cross-linking and bundling by varying the scruin concentration, $c_S$, for a fixed actin concentration, $c_A$, such that the density of cross-links, $R$, is $c_S/c_A$ and varies from 0 to 1; a pelleting assay confirms that the degree of polymerized actin remains constant for a given $c_A$ as $R$ is varied (19). The morphology of actin-scruin networks remains similar to that of an entangled F-actin solution with values of $R$ up to 0.03. For $R > 0.03$, we observe the formation of compact bundles (Fig. 1C); the bundle thickness increases even further as $R$ is increased, as shown for $R = 0.5$ in Fig. 1D. Using electron microscopy, we measure the average bundle diameter, $D_B$, as a function of $R$; for $R > 0.03$, $D_B$ varies approximately as $D_B \approx R^x$, where $x \simeq 0.3$ (19). For $R = 1$, the average bundle thickness is $D_B \approx 50$ nm, which leads to a significant increase in the rigidity of the actin bundles. The bending rigidity of any rod increases rapidly with its width, varying as $D^4$ (21), and for scruin-mediated actin bundles, $\kappa_B \simeq \kappa_o(D_B/D)^4$, consistent with theory (17). Thus, the average bundle stiffness increases to $\sim 600\kappa_o$, greatly increasing the persistence length. We can also directly control the average distance between filaments, $\xi$, by varying both $R$ and $c_A$ (22),

$$\xi \sim D_B/\sqrt{c_A} \sim R^x/\sqrt{c_A} \qquad (1)$$

Thus, we can finely tune the network morphology.

To measure the elasticity of these networks, we apply a force and measure the resultant deformation; the elastic modulus, $G'$, is defined as the ratio of the stress, $\sigma$, or force per unit area, to the strain, $\gamma$; thus, $G' = \sigma/\gamma$. The networks can also have a viscous or dissipative response, and the resultant stress depends on the strain rate, $\dot{\gamma}$, defining the loss modulus, $G'' = \sigma/\dot{\gamma}$. More generally, $G'(\omega)$ and $G''(\omega)$ depend on the frequency and are measured by applying a small oscillatory stress at a frequency, $\omega$. In these cross-linked networks, the elastic modulus dominates the mechanical response, reaching a frequency-independent plateau, $G_o$, at frequencies less than 1 Hz (fig. S1). The magnitude of $G_o$ is highly dependent on the morphology of the network; for a small amount of cross-linking, the composite network is a soft elastic gel, and $G_o$ decreases weakly as $R$ decreases below 0.03 (Fig. 2A). However, for $R > 0.03$, $G_o$ increases dramatically with $R$. Thus, the elasticity is strongly dependent on the scruin-mediated interactions that cross-link and bundle actin filaments, even at the same $c_A$.

The magnitude of $G_o$ is also highly dependent on actin concentration for a fixed value of $R$. For $R = 0.12$, we measure $G_o \sim c_A^\alpha$, where $\alpha \approx 2.5$ as shown by the open triangles in Fig.

**Fig. 1. (A)** Schematic representation of the state diagram of cross-linked and bundled F-actin networks, showing the variations in the elasticity of the networks with changes in actin concentration, $c_A$, or density of cross-linking $R = c_S/c_A$, where $c_S$ is the scruin concentration. By varying either $c_A$ or $R$, the elastic modulus, $G_o$, can be varied by more than three orders of magnitude, from less than 0.1 Pa to 300 Pa. For large values of $c_A$ or $R$ (indicated by the red plane), the network elasticity becomes nonlinear at very small deformations, and the elasticity becomes strain dependent and increases markedly upon increased strain. By contrast, at very low values of $c_A$ or $R$ (indicated by the blue plane), the network mechanical response remains linear up to large strains, and no strain stiffening is observed. Transitions between these two regimes of elasticity can be made by changing either $R$ or $c_A$, as indicated by the dashed lines. **(B to D)** Confocal microscope images of actin networks, $c_A = 11.9$ μM, labeled with Texas Red–phalloidin as a function of $R$. **(B)** $R = 0$, **(C)** $R = 0.07$, **(D)** $R = 0.5$. As $R$ is increased for a fixed $c_A$, actin filaments are cross-linked into tight bundles. The average bundle thickness is weakly proportional to $R$ between $R = 0.03$ and $R = 1$. Because the total filament concentration remains constant, the average mesh size also increases. Bar (B), 3 μm. The bright circles in (B) to (D) are 1-μm-diameter colloidal particles.

2C, which is consistent with all proposed theoretical network models to within our experimental uncertainty (*12, 23, 24*). We see similar scaling for all values of $R$, as shown in Fig. 2C for weakly cross-linked networks, $R = 0.03$ (squares), and thickly bundled networks, $R = 0.3$ (circles). Thus, the elastic modulus is also strongly dependent on the filament density.

The elasticity of the networks can also exhibit a marked dependence on applied strain, $\gamma$. In the regime where $G_o$ increases rapidly with $R$ (Fig. 1A), the elastic modulus is linear below a critical strain, $\gamma_{crit} \sim 10\%$. However, above this strain, $G_o$ increases dramatically over a very small change in $\gamma$ up to a maximum strain, $\gamma_{max}$, whereupon the network breaks irreversibly (Fig. 2B, inset). This strain stiffening is completely reversible and the network can be cycled through strains up to $\gamma_{max}$ without any history dependence of the elastic response. These composite networks constitute an exceptional material, whose modulus increases significantly with virtually no change in $\gamma$; thus, they have a nearly vanishing compliance for $\gamma > \gamma_{crit}$.

The origin of the elasticity of entangled F-actin solutions is purely entropic, even though the filaments are semiflexible, with a rather large bending rigidity (*25, 26*). Thus, the elasticity arises because an applied strain reduces the accessible fluctuations; this is an entropic elasticity, similar to that of flexible polymers such as rubber. However, when filaments are chemically cross-linked into networks such that the distance between cross-links, $\ell_c$, is less than $\ell_p$, or when the persistence length is increased as a result of bundling, it is unclear whether the network elasticity originates from the actual bending of filaments, which is an enthalpic elasticity, or from stretching out thermal fluctuations of the filaments, which is an entropic elasticity (*12, 23, 24*).

To delineate the role of entropic effects in network elasticity, we model the network as a collection of thermally fluctuating, semiflexible filament segments of length, $\ell_c$, the average distance between cross-links, such that $\xi \leq \ell_c \ll \ell_p$. Thermally driven transverse fluctuations reduce the end-to-end filament extension and lead to an entropic spring; for small extensions, the force, $F$, required to extend this spring by length $\delta\ell$ is $F \sim (\kappa_B^2/k_B T \ell_c^4)\delta\ell$, where $k_B T$ is the thermal energy (*12*) (fig. S2); this is the wormlike chain model that also describes the behavior of DNA (*27*). Accounting for the concentration of chain segments through the mesh size, we can calculate the resultant stress (*8*), $\sigma = F/\xi^2$, and thereby determine the linear elastic modulus of the network by applying a strain, $\gamma \sim \delta\ell/\ell_c$. We find (*12*) (fig. S3)

$$G_o \sim \frac{\sigma}{\gamma} \sim \frac{\kappa_B^2}{k_B T \xi^2 \ell_c^3} \qquad (2)$$

We assume that, for a fixed $R$, $\ell_c$ is directly proportional to the distance between filament entanglements (*12, 28*) (fig. S3). Thus, $G_o \sim$

$c_A^{11/5}$, which depends strongly on actin concentration, consistent with that observed for both weakly cross-linked networks, $R = 0.03$, and for thickly bundled networks, $R = 0.3$. We conclude that the elastic stiffness of both weakly cross-linked and thickly bundled actin networks is entropic in origin, originating from the stretching out of thermal fluctuations of individual actin filaments (Fig. 3).

A critical test of this picture for the origin of the elasticity is the strain dependence; when an entropic, semiflexible network is extended, thermally induced transverse fluctuations are pulled out. At sufficiently large extension, the response ceases to be linear, consistent with our observed strain stiffening above $\gamma_{crit}$. Entropic, semiflexible networks break at an applied strain that is expected to decrease weakly with increasing filament concentration (*12*) (fig. S3); this is also consistent with our observations, as shown in Fig. 2D. We can quantitatively test our model for the elasticity by determining the divergence of the stress response in the nonlinear elastic regime. Here, the force required to extend a single semiflexible filament, $F \sim 1/(\ell_c - \ell)^2$, diverges dramatically as full extension is approached, where $\ell \rightarrow \ell_c$ (*27, 29*). However, the extreme nonlinearity of the modulus makes precise oscillatory strain measurements virtually impossible, because the measured stress waveforms become highly nonsinusoidal. To overcome this limitation, we superpose a small oscillatory stress of magnitude $\delta\sigma$, for a constant applied stress, $\sigma_o$, with $\delta\sigma/\sigma_o < 0.1$ at 0.1 Hz, and determine the
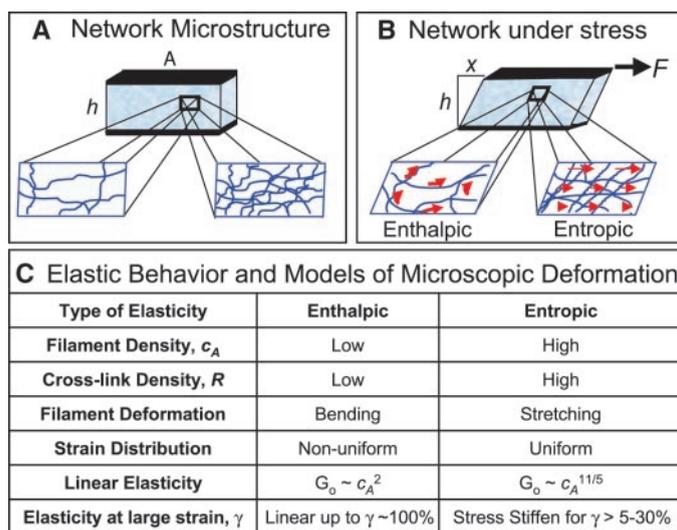
differential elastic modulus, $K'(\sigma_o) = [\delta\sigma/\delta\gamma]|_{\sigma_o}$ as a function of $\sigma_o$. This measurement applies a constant prestress while measuring the response to a small oscillatory stress, allowing us to accurately probe the divergence of the response as a function of applied prestress.

When the elastic modulus is strain-independent, the differential modulus is the same as the elastic modulus, $K'(\sigma_o) = G_o$. However, above the critical stress, $\sigma_{crit} = G_o\gamma_{crit}$, $K'$ increases markedly until the network breaks, as shown for a large range of actin concentrations at fixed $R$ in Fig. 4. In this stress stiffening regime, $K'(\sigma_o) \sim \sigma_o^{3/2}$, consistent with that predicted for a single semiflexible polymer, $dF/d\ell \sim F^{3/2}$ (*27, 29*). The theoretical form of $K'(\sigma_o)$ for these networks is predicted by using the full force-extension relation of a single actin filament and taking into account variations in $\ell_c$ and $c_A$, as well as spatial averaging of the orientation of chain segments (*19*). By scaling the theory to fit the data for one concentration, $c_A = 29.4$ μM and $R = 0.03$, we determine $\ell_c$ and calibrate the absolute stress; the theory is then in excellent accord with the remaining data sets, with no additional adjustable parameters, as shown by the curves in Fig. 4. Moreover, the theory suggests that the functional form of the data should be the same for all values of $c_A$ and $R$. Consistent with this prediction, all the data can by scaled onto a single master curve (Fig. 4, inset). This provides conclusive support for our hypothesis that the origin of both the linear and the nonlinear elasticity of the network is due to stretching of thermal fluctuations of single fil-
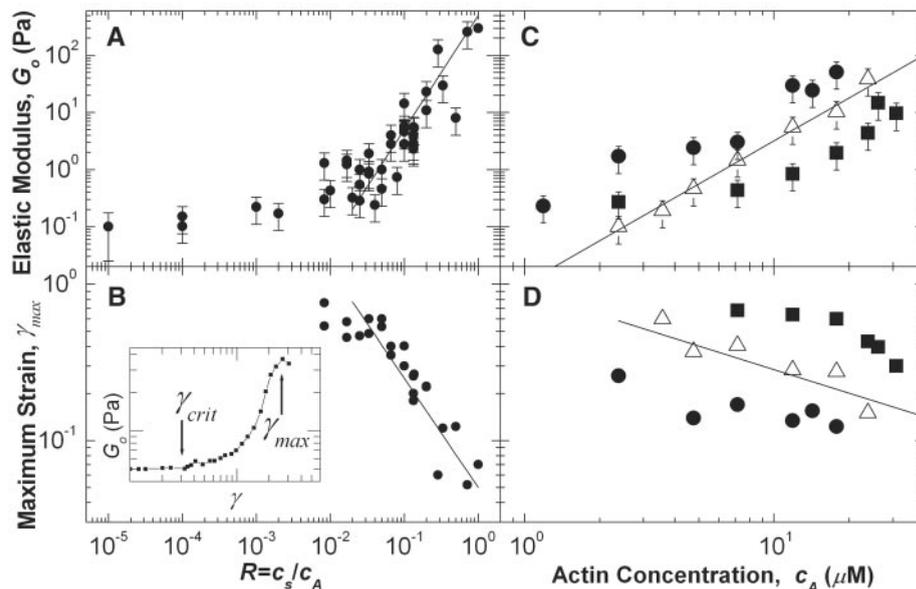


**Fig. 2.** The elastic modulus, $G_o$, and maximum strain, $\gamma_{max}$, as a function of $R$ and $c_A$. (**A**) $G_o$ as a function of $R$ for $c_A = 11.9$ μM. The solid line indicates a scaling of $G_o \sim R^2$. (**B**) $\gamma_{max}$ versus $R$ for $c_A = 11.9$ μM. The solid line indicates $\gamma_{max} \sim R^{-0.6}$. (Inset) Typical strain stiffening response for a composite network with $c_A = 11.9$ μM and $R = 0.03$, indicating the onset of nonlinear elastic response, $\gamma_{crit}$, and the maximum strain, $\gamma_{max}$, before the network breaks. (**C**) $G_o$ as a function of $c_A$ for $R = 0.03$ (■), 0.13 (△), and 0.3 (●). The solid line shows a scaling of $c_A^{2.5}$ and the error bars indicate our sample-to-sample reproducibility. (**D**) $\gamma_{max}$ as a function of $c_A$ for the same values of $R$. The solid line shows a scaling of $c_A^{-0.5}$.

**Fig. 3.** A summary of the interpretation of results presented in this paper. (**A**) Networks are polymerized between two plates of area, $A$, and separation, $h$. By varying the filament or cross-link concentration, we vary the network microstructure; low filament and cross-link density are shown in the left cartoon, whereas high filament and cross-link density are shown in the right cartoon. (**B**) We measure the mechanical properties of the networks by applying a force, $F$, per unit area, $A$, or stress and measuring the deformation or strain $\gamma \equiv x/h$. The microscopic distribution of the strain differs in the networks. Our data show two distinct mechanical regimes, distinguished by their nonlinear response. One of these is consistent with macroscopic mechanical properties due to enthalpic filament bending, as expected for low cross-link or filament density. This leads to a highly inhomogeneous distribution of strain, as indicated by the red arrows. By contrast, the mechanical properties of dense networks are consistent with stretching of thermally induced filament fluctuations and an entropic elasticity. The resultant strain is uniform throughout the sample, as indicated by the red arrows. (**C**) The table summarizes the essential differences in the elasticity of entropic and enthalpic networks.

**A** Network Microstructure

**B** Network under stress

Enthalpic   Entropic

**C** Elastic Behavior and Models of Microscopic Deformation

| Type of Elasticity | Enthalpic | Entropic |
|---|---|---|
| Filament Density, $c_A$ | Low | High |
| Cross-link Density, $R$ | Low | High |
| Filament Deformation | Bending | Stretching |
| Strain Distribution | Non-uniform | Uniform |
| Linear Elasticity | $G_o \sim c_A{}^2$ | $G_o \sim c_A{}^{11/5}$ |
| Elasticity at large strain, $\gamma$ | Linear up to $\gamma \sim 100\%$ | Stress Stiffen for $\gamma > 5\text{-}30\%$ |

**Fig. 4.** The differential elastic modulus, $K'$, as a function of applied steady shear stress, $\sigma_o$, for $R = 0.03$ and several values of $c_A$; the lines through the data indicate theoretical predictions for each concentration determined from the single-filament response. The values of $c_A$ are 29.4 μM (▲—), 21.4 μM (●- -·), 11.9 μM (■- -), and 8.33 μM (◆···). The stress stiffening response of a bundled network, $R = 0.5$, at $c_A = 7$ μM is also shown (○). The dotted line at the right indicates $\sigma_o{}^{3/2}$. (**Inset**) The data sets rescaled by $\sigma_{crit}$ and $G_o$ showing the universal form of the stress stiffening response; the rescaled theory is indicated by the solid line.
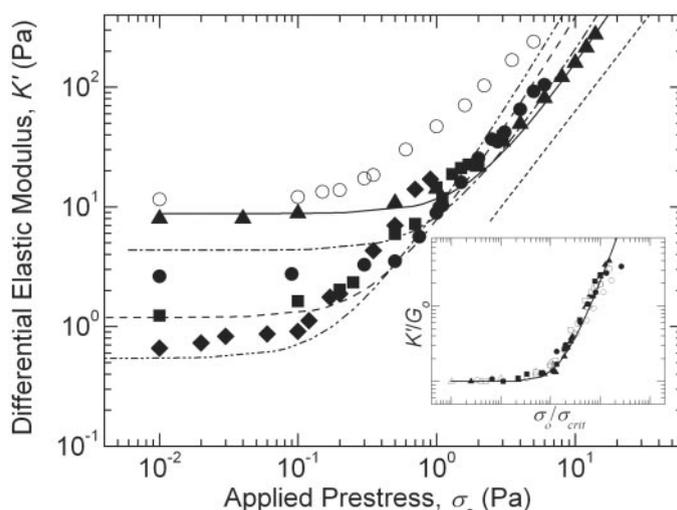
**Fig. 5.** The $R$-$c_A$ state diagram of actin:scruin networks detailing the tunability of $G_o$; colors indicate a range from 0.03 Pa (purple) to 300 Pa (red), as shown by the legend. Symbols differentiate networks that stress stiffen (+) from those that do not (○).
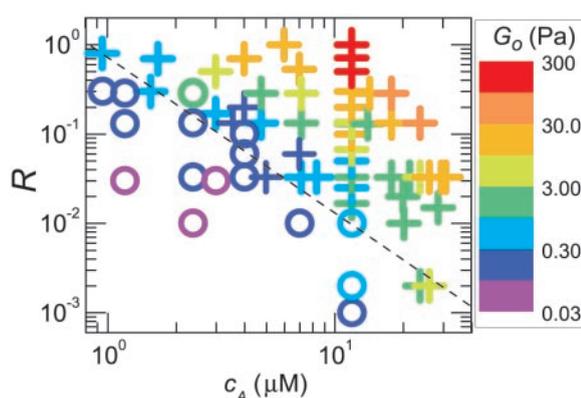
aments. Thus, the elastic stiffening of the network results from the nonlinear force-extension behavior of individual filaments; this further supports our hypothesis that the elasticity of cross-linked actin networks is entropic in origin.

The origin of the network elasticity appears to remains entropic, even as $\kappa$ increases as a result of bundling, or as $\ell_c$ decreases as a result of increased cross-linking. We demonstrate this by tuning these two parameters simultaneously, by varying $R$ while keeping $c_A$ fixed. The resultant networks exhibit variations in both $G_o$ and $\gamma_{max}$ with $R$ that are consistent with our model (fig. S3). They also exhibit similar strain stiffening, and the qualitative form of the divergence of the incremental modulus remains unchanged. For a given $c_A$, the modulus increases as $G_o \sim R^2$, and the critical strain simultaneously decreases as $\gamma_{max} \sim R^{-0.6}$ (Fig. 2). Interestingly, two networks can have the same $G_o$ for different actin concentrations, provided that $R$ varies; however, the onset of nonlinear behavior occurs at a different $\sigma_{crit}$, as shown by the open circles in Fig. 4. Thus, changes in the network morphology caused by variation in the filament cross-linking and bundle thickness dramatically affect both the linear and nonlinear elastic behavior.

At very low values of $c_A$ or $R$, the qualitative features of the elastic response change dramatically. This is most pronounced at very low values of $R$, where $G_o$ exhibits virtually no dependence on $R$ (Fig. 2A). Furthermore, these networks do not exhibit any strain stiffening but instead deform easily upon increased applied stress, and the elastic response remains linear for strains as large as $\gamma \sim 1$. This suggests that there is a second regime of elasticity with a qualitatively different origin. To capture the full variety of elastic behavior, we summarize all the data in the $c_A$-$R$ state diagram (Fig. 5). The elastic modulus varies continuously over four orders of magnitude as both $c_A$ and $R$ are varied. We delineate the two distinct regimes with different symbols. In the first regime, for sufficiently large $c_A$ or $R$, $G_o$ is highly sensitive to both $c_A$ and $R$ and exhibits pronounced strain stiffening (denoted by the plus signs in Fig. 5). The origin of the mechanical response is quantitatively explained by our model of entropic elasticity, which reflects the stretching and compression of individual filaments. This model implicitly assumes that the deformations of the network are affine, or distributed uniformly throughout the sample, and thus the strain is homogeneous at all length scales (Fig. 3). There is a sharp transition, denoted by the dashed line in Fig. 5, to the second regime of elasticity, where $G_o$ is much less sensitive to both $c_A$ and $R$ and exhibits no strain stiffening (denoted by the open circles in Fig. 5). This behavior is consistent with a model that suggests that the network deformation at lower filament or cross-link concentrations may be nonaffine; the elastic connections of the network are sparse, and its response is dominated by bending of indi-

vidual filaments in isolated locations, leading to a highly inhomogeneous strain of the network (*13, 14*) (Fig. 3). In this model, the linear modulus is predicted to be $G_o \sim c_A^2$ (*23, 24*). Furthermore, because network elasticity is determined by filament bending, which is rather small on the molecular scale, there is no mechanism for strain stiffening. Thus, as summarized in Fig. 5, a network of rigidly cross-linked semiflexible polymers can exhibit a rich variety of elastic behaviors simply by varying the filament concentration, cross-link density, or bundle thickness.

We speculate that there may also be a third regime of elasticity, in the limit of very high values of $c_A$ and $R$; here, the response will again be affine but will be totally enthalpic in nature, and the compliance will be dominated by the mechanical stretching and compression of filaments or bundles, with no universal mechanism for strain stiffening. Our results also have important implications for how a cell may regulate its mechanical response, with small variations in either filament or cross-link concentration to make rapid and precise transitions to qualitatively alter the mechanical strength of the cytoskeletal network. Furthermore, the mechanical properties of the cytoskeletal actin network may also be varied as a function of external prestress, providing a potential mechanism for mechanosensing and mechanoprotection in the cell by allowing small variations in force to significantly increase its mechanical strength. Finally, our data highlight the importance of understanding single-molecule mechanics to interpret the mechanical properties of networks. Because we can so precisely parameterize the elastic behavior of cross-linked actin networks, it is now possible to be quantitatively predictive for in vivo physiological conditions. Other physiological cross-linkers, unlike scruin, are neither rigid nor inextensible; as a result, the single-molecule elasticity and dynamics of the cross-linker must also be included when modeling these more complex networks. However, our data using the rigid cross-linker scruin provide an essential benchmark for the elasticity of the cytoskeletal actin network.

### References and Notes

1. H. Lodish *et al.*, *Molecular Cell Biology* (Freeman, New York, ed. 4, 1999).
2. T. Kreis, R. Vale, *Cytoskeletal and Motor Proteins* (Oxford Univ. Press, Oxford, ed. 2, 1999).
3. F. Gittes, B. Mickey, J. Nettleton, J. Howard, *J. Cell Biol.* **120**, 923 (1993).
4. P. A. Janmey, S. Hvidt, J. Lamb, T. P. Stossel, *Nature* **345**, 89 (1990).
5. R. Ruddies, W. H. Goldmann, G. Isenberg, E. Sackmann, *Eur. Biophys. J.* **22**, 309 (1993).
6. P. A. Janmey *et al.*, *J. Biol. Chem.* **269**, 32503 (1994).
7. T. D. Pollard, J. A. Cooper, *Annu. Rev. Biochem.* **55**, 987 (1986).
8. J. Ferry, *Viscoelastic Properties of Polymers* (Wiley, Indianapolis, ed. 3, 1980).
9. D. H. Wachsstock, W. H. Schwarz, T. D. Pollard, *Biophys. J.* **66**, 801 (1994).
10. M. Tempel, G. Isenberg, E. Sackmann, *Phys. Rev. E* **54**, 1802 (1996).
11. J. Y. Xu, D. Wirtz, T. D. Pollard, *J. Biol. Chem.* **273**, 9570 (1998).
12. F. C. MacKintosh, J. A. Kas, P. A. Janmey, *Phys. Rev. Lett.* **75**, 4425 (1995).
13. D. A. Head, A. J. Levine, F. C. MacKintosh, *Phys. Rev. Lett.* **91**, 108102 (2003).
14. J. Wilhelm, E. Frey, *Phys. Rev. Lett.* **91**, 108103 (2003).
15. J. Xu *et al.*, *Biophys. J.* **74**, 2731 (1998).
16. L. G. Tilney, *J. Cell Biol.* **64**, 289 (1975).
17. J. H. Shin, L. Mahadevan, P. T. So, P. Matsudaira, *J. Mol. Biol.* **337**, 256 (2004).
18. M. B. Sherman *et al.*, *J. Mol. Biol.* **294**, 139 (1999).
19. J. H. Shin, M. L. Gardel, L. Mahadevan, P. Matsudaira, D. A. Weitz, in preparation.
20. Materials and methods are available as supporting material on *Science* Online.
21. L. D. Landau, E. M. Lifshitz, *Theory of Elasticity* (Pergamon, Oxford, ed. 3, 1986).
22. C. F. Schmidt, M. Barmann, G. Isenberg, E. Sackmann, *Macromolecules* **22**, 3638 (1989).
23. K. Kroy, E. Frey, *Phys. Rev. Lett.* **77**, 306 (1996).
24. R. L. Satcher, C. F. Dewey, *Biophys. J.* **71**, 109 (1996).
25. H. Isambert, A. C. Maggs, *Macromolecules* **29**, 1036 (1996).
26. D. C. Morse, *Macromolecules* **31**, 7044 (1998).
27. C. Bustamonte, J. F. Marko, E. D. Siggia, S. Smith, *Science* **265**, 1599 (1994).
28. A. N. Semenov, *J. Chem. Soc. Faraday Trans. 2* **82**, 317 (1986).
29. M. Fixman, J. Kovac, *J. Chem. Phys.* **58**, 1564 (1973).
30. We gratefully acknowledge support from the NSF (DMR-0243715), the Materials Research Science and Engineering Center through the auspices of the NSF (DMR-0213805), Lucent Graduate Research Program for Women fellowship (M.L.G.), NIH GM52703 (P.M.), NIH Supplementary grant (L.M.), and NSF Graduate Research fellowship (J.H.S.). We thank A. R. Bausch for actin samples and G. Waller for providing technical assistance in scruin purification.

# A Microfluidic Device for Conducting Gas-Liquid-Solid Hydrogenation Reactions

**Juta Kobayashi,[1] Yuichiro Mori,[1] Kuniaki Okamoto,[1] Ryo Akiyama,[1] Masaharu Ueno,[2] Takehiko Kitamori,[2] Shū Kobayashi[1]\***

We have developed an efficient system for triphase reactions using a microchannel reactor. Using this system, we conducted hydrogenation reactions that proceeded smoothly to afford the desired products quantitatively within 2 minutes for a variety of substrates. The system could also be applied to deprotection reactions. We could achieve an effective interaction between hydrogen, substrates, and a palladium catalyst using extremely large interfacial areas and the short path required for molecular diffusion in the very narrow channel space. This concept could be extended to other multiphase reactions that use gas-phase reagents such as oxygen and carbon dioxide.

Multiphase catalytic reactions play important roles not only in the research laboratory but also in the chemical and pharmaceutical industries (*1*). They are classified according to the phases involved, such as gas-liquid, gas-liquid-liquid, or gas-liquid-solid reactions. Although numerous multiphase catalytic reactions are known and many are used in industry, these reactions are still difficult to conduct when compared to homogeneous reactions, because the efficiency of interaction and mass transfer between different phases is extremely low, and thus in most cases the reaction rates are slow. In general, to accelerate multiphase catalytic reactions, some treatment producing high interfacial area between the two or three reacting phases, such as vigorous stirring or additional equipment, is needed, and the development of more effective, simple devices that can produce such a high interfacial area between different phases is a much-sought-after goal.

To achieve efficient multiphase catalytic reactions, we focused on a new device, which has a very small channel (nanometer- to micrometer-sized in width and depth and centimeter- to meter-sized in length) in a glass plate (*2–10*). A similar device, the so-called "microchannel reactor," is used mainly in the field of analytical chemistry (*11*). The device has a very large specific interfacial area per unit of volume. In concrete figures, this area rises to $10,000 \sim 50,000$ m$^2$/m$^3$, as opposed to only 100 m$^2$/m$^3$ for conventional reactors used in chemical processes (*12*). Our idea is to immobilize a solid catalyst on the

[1]Graduate School of Pharmaceutical Sciences, The University of Tokyo, 7-3-1 Hongo, Bunkyo-ku, Tokyo, 113-0033, Japan. [2]Department of Applied Chemistry, Graduate School of Engineering, The University of Tokyo, 7-3-1 Hongo, Bunkyo-ku, Tokyo, 113-8656, Japan.

\*To whom correspondence should be addressed. E-mail: skobayas@mol.f.u-tokyo.ac.jp

**Materials and Methods**

Samples are prepared by gently mixing purified scruin (*1, 2*), G-buffer (2 mM Tris HCl, 0.2 mM ATP, 0.2 mM $CaCl_2$, 0.2 mM DTT, 0.005% $NaN_3$, pH 8.0) and 10x F-actin polymerization buffer (F-buffer, 2mM Tris HCl, 2mM $MgCl_2$, 100mM KCl, 0.2mM DTT, 0.2mM $CaCl_2$, 0.5mM ATP, pH 7.5).  G-actin is added last to initiate network formation; the final solution is mixed for 10 seconds and then loaded into the sample chamber.

For confocal microscopy, solutions are loaded into glass chambers and incubated with Texas-Red phalloidin, polymerized for one hour at ~25 ˚C and imaged with a Zeiss LSM 510-Meta confocal microscope; images are deconvolved using Huygens2 software (SVI, Inc).

For bulk rheology, the solution is loaded in a stress-controlled rheometer (Bohlin C-VOR) with 40 mm parallel plate geometry and a 160 $\mu$m gap thickness; this geometry enables measurements with a total sample volume of only 300 $\mu$L and stress resolution of 0.0059 Pa.  Steady state behavior is achieved after polymerizing *in situ* for one hour at 25 °C, and no further time evolution is observed during our experiments.  Further tests confirm that the linear elastic modulus is independent of specific measurement geometry.

**Supporting Figures**
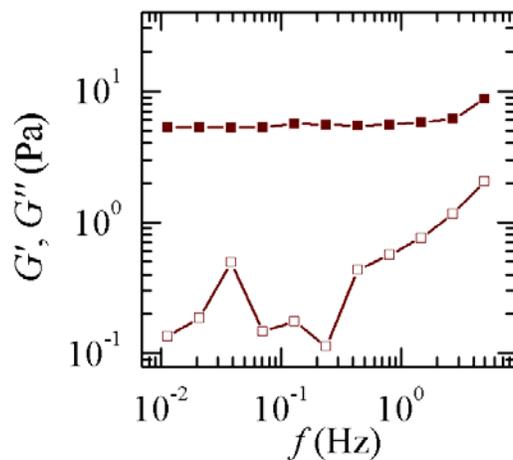


**FIG S1. Frequency Dependence of Elastic Modulus**

The elastic modulus, $G'$ (closed squares), and loss modulus, $G''$ (open squares), as a function of frequency for $c_A$=11.9 $\mu$M and $R$=0.13. The qualitative form of the frequency dependent moduli is similar for all networks. In all cases, the elastic modulus is nearly frequency independent and dominates the viscoelastic response.
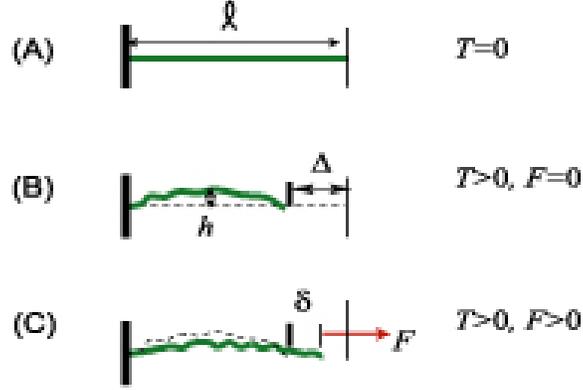
**FIG S2. Scaling of the linear entropic spring constant of a semi-flexible polymer.**

We examine a single, inextensible, semi-flexible filament with a fixed total contour length, $\ell_c$ and bending stiffness, $\kappa_o$. pinned to a rigid wall on one end and the other free to fluctuate: (A) at absolute zero temperature (T=0) where thermal effects vanish, the end-to-end distance, $\ell$, is identical to $\ell_c$. (B) for T>0, transverse thermal fluctuations of the filament with a magnitude, $h$, result in a contraction of end-to-end chain length by $\Delta \sim h^2/\ell$. The magnitude of $\Delta$ can be estimated by equating thermal energy per unit length, $k_B T/\ell$ to the bending energy per length, $U_B \sim \kappa \left(h/l^2\right)^2$. Thus, $\Delta \sim \ell^2 k_B T/\kappa$.

(C) An extensional force, $F$, partially extends the contracted filament by a length, $\delta \ell$, resulting in a decrease in the magnitude of transverse fluctuations. The resultant energy per length is $U_F \sim F\left(h/l\right)^2$. Thus, under an applied force, $U_B + U_F = k_B T/\ell$ determines the magnitude of the thermal fluctuations. Because the contour length of the filament is fixed, we determine $\left(h/\ell\right)^2 \sim \left(\Delta - \delta \ell\right)/\ell$. Thus, the linear force-extension of the filament is $F \sim \left(\kappa^2/\left(k_B T \ell^4\right)\right)\delta \ell$.
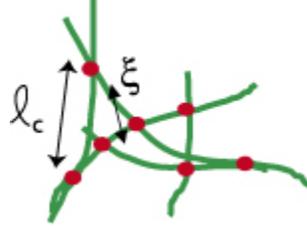
**FIG S3. Scaling of Entropic Network Elasticity with $c_A$ and $R$**

*Origin of Network elasticity and scaling with $c_A$.* We consider a network of semiflexible filaments with a persistence length, $\ell_p \sim \kappa/(k_B T)$ and a concentration, $c_A$ as shown by the cartoon of a semi-flexible polymer network. The average mesh size is $\xi \sim 1/\sqrt{c_A}$. We consider dense networks where $\xi \ll \ell_p$. Rigid, inextensible crosslinks between neighboring filaments are separated by a distance, $\ell_c$. This distance between crosslinks is proportional to the entanglement length (3), $\ell_c \sim n\ell_e \sim n\xi^{4/5}\ell_p^{1/5}$ where $n$ is determined by the number of crosslinks in solution. To determine the maximum strain associated with pulling out all thermal fluctuations, we consider the strain at complete extension of the filaments, $\gamma_{max} \sim \Delta/\ell_c \sim \ell_c/\ell_p$. For a constant $R$, this predicts that the maximum strain decreases weakly with filament concentration: $\gamma_{max} \sim 1/c_A^{2/5}$. We also observe that the onset of stress stiffening regime, $\gamma_{crit} \sim \gamma_{max}$. Under an applied force, $F$, and single filament elongation, $\delta$, the stress imposed on the network is $\sigma \sim F/\xi^2$ and the strain on each filament is $\gamma_{max} \sim \delta/\ell_c$. Thus, the modulus

$$G_o \sim \sigma/\gamma \sim \kappa^2/\left(k_B T \xi^2 \ell_c^3\right) \tag{1}$$

or, at a given crosslink density, $G_o \sim c_A^{11/5}$.

*Scaling with R.* To elucidate variations in network elastic response as a function of crosslinking and bundling, we tune these two parameters simultaneously by varying $R$ while maintaining $c_A$=11.9 $\mu$M. Using the electron microscopy data, we directly measure $D_B \sim DR^x$ where $x \cong 0.2$ for $R$>0.03. Due to the compact nature of the scruin cross-linking and the large number of scruin-scruin interactions between two filaments, the bending energy of individual actin filaments bundled with scruin is proportional to $\kappa_B \sim \kappa_o(R^x)^4$ (*4*), as expected for a homogeneous rigid rod. As the average bundle thickness increases, the mesh size must also increase, $\xi \sim D_B / c_A^{1/2} \sim DR^x / c_A^{1/2}$. We directly measure $x \cong 0.3$ from both the confocal data and multiple particle tracking data (*2*). Thus, we average these two measured values to obtain $x \cong 0.25$

Furthermore, because the number of crosslinks increases with $R$, the distance between these crosslinks also decreases, and we assume that $\ell_c \sim \xi R^{-y}$. By inserting this scaling into (1), we predict that $G_o \sim c_A^{11/5} R^{(6x+15y)/5}$. We measure $G_o \sim R^2$, as shown in Fig. 1A; this allows us to determine the effect of cross-linking, $y \simeq 0.58$.

Using these values of $y$ and $z$, we predict that $\gamma_{max} \sim R^{-1}$; this is compared to our data as shown by the circles in Fig 2B, where the line indicates a scaling of $R^{-0.6}$. Thus, we find that entropic elasticity of both single filaments and small bundles of filaments dominate both the linear and nonlinear mechanical response over a large range of crosslink densities and bundle thicknesses for a constant filament density.

1. S. J. Sun, M. Footer, P. Matsudaira, *Molecular Biology of the Cell* **8**, 421 (1997).
2. J. H. Shin, M. L. Gardel, L. Mahadevan, P. Matsudaira, D. A. Weitz, *to be published* (2003).
3. A. N. Semenov, *J. Chem. Soc. Faraday Trans. 2* **82**, 317 (1986).
4. J. H. Shin, L. Mahadevan, G. Waller, K. Langsetmo, P. Matsudaira, *Journal of Cellular Biology* **162**, 1183 (2003).